Evaluation of Various Flow Control Methods in Reducing Drag and Aerodynamic Heating on the Nose of Hypersonic Flying Objects

S. Abbasi[†] and S. Esmailzadeh Vali

Department of Mechanical Engineering, Arak University of Technology, Arak, Iran

†Corresponding Author Email: s_abbasi@arakut.ac.ir

ABSTRACT

Effective deduction of air heating load and drag is a critical issue in hypersonic vehicle engineering applications. In this research, seven various geometrical models have been proposed to study and compare the effect of each configuration on the flow field, drag, and aerodynamic heating deduction under the same flow conditions. The presented configurations in this study: (a) blunt-body geometry as a reference of comparison, (b) blunt-body geometry with a spike, (c) blunt-body geometry with an counter flow jet, (d) blunt-body geometry with a spike and counter flow jet, (e) blunt-body geometry with a spike and aerodisk, (f) blunt-body geometry with a spike, aerodisk, and root counter flow jet, (g) blunt-body geometry with a spike, four aerodisks and root counter flow jet. The Reynolds-Averaged equations have been solved using the Finite Volume Method (FVM) along with the shear stress turbulence model (k-ω SST). The flow is assumed compressible, steady-state, and axisymmetric with a free stream Mach number of 6. According to the study of each configuration's performance related to the parameters of drag, maximum pressure, and maximum heat flux factors on the blunt-body walls, (g) configuration with a drag factor of 0.2699, maximum pressure factor of 209.8, and maximum heat flux factor of 25.1, has the most deduction on the blunt-body walls among the seven configurations. The deduction percentage of drag, maximum pressure, and maximum heat flux factors of (g) configuration to (a) configuration are %72.1, %94.5, and %79.9, respectively, which significantly diminished drag and heat flux. Also, the best configuration scenarios for drag and aerodynamic heating deduction are geometrical models of g, f, d, e, c, b, and a, respectively.

1. INTRODUCTION

Thanks to technology enhancements, humankind has achieved the ability to move objects with hypersonic velocities. The design and construction of the jet engine was beginning to open the gates of aerospace science, which challenges the scientists of this field in many cases. The capability of jet engine construction to make an object reach hypersonic, has been impressively improved. Afterward, due to drag, and aerodynamic heating occurrence in moving objects, scientists started to research thermal protection systems.

The blunt nose configuration is used in hypersonic vehicle designs because it diminishes the air heat flux at the stagnation point and prepares better operating conditions for the crew or searching systems by using more space inside the vehicle (Ahmed & Qin, 2020).

Nowadays, reducing and controlling drag and aerodynamic heating using thermal protection systems has gained great attention. Since the produced aerodynamic heating caused by compression and friction between the surface and the atmospheric gas leads to damage and destruction of the object's nose, which moves inside the hypersonic flow field, the necessity of employing thermal protection systems is quite apparent (Anderson Jr et al., 1991). Furthermore, drag and aerodynamic heating, which have effects on the nose of the objects in hypersonic flights, stem from a strong bow shock in front of the nose. Hence, one could simultaneously diminish both drag and aerodynamic forces by restoring the flow field in front of the flying object's nose to weaken the bow shock (Ahmed & Qin, 2020). The presence of a strong shock in front of the blunt nose in a hypersonic flow field creates many difficulties in the stagnation zone of the flow field.

Therefore, the bow shock has the most intensity close to the central zone because the flow in this area has the most vortex flow characteristics, which leads to a subsonic zone generation. Nevertheless, with moving along the blunt nose surface, the flow vorticity and the bow shock intensity in the same proportion are diminished, and the flow could gain higher hypersonic velocities behind the bow shock, which is maximum at the surface edge. For this purpose, regarding drag and great aerodynamic heating in front of the blunt nose, researchers have tried to find solutions for attenuating drag and aerodynamic heating (Fujii et al., 2013).

In all of the proposed methods, the aim is to convert the strong bow shock into a collection of weakened oblique shocks. The first presented approach for reducing drag is to use the spike in front of the blunt nose (Piland & Putland, 1956; Mehta, 2000; Panaras & Drikakis, 2009; Mansour & Khorsandi, 2014). Afterward, employing the combination of a spike and aerodisk was commonly used to control drag (Tahani et al., 2013; Yadav et al., 2018; Zhong et al., 2019; Tembhurnikar et al., 2020). Using the counter flow jet flow (Li et al., 2018; Rashid et al., 2019; Sharma & Nair, 2020; Ji et al., 2021; Renane et al., 2022; Wang & Zhang, 2022) and a forward-facing cavity flow (Silton & Goldstein, 2005; Seiler et al., 2007; Saravanan et al., 2009; Rashid et al., 2021; Xie et al., 2021) are among other flow control approaches in hypersonic noses. In the next step, hybrid methods were employed to diminish drag (Qin & Xu, 2019; Huang & Yao, 2020; Ma et al., 2020; Zhang et al., 2022). Among these methods, spike implementation in front of the blunt nose was proposed by Alexander (1947) for the first time, which is considered as the simplest suggested method until now.

Mair (1952) experimentally studied the spiked flat-face cylinder and spike-nose hemisphere-cylinder models with the Mach number of 1.96 and the Reynolds number of 1.65×10^5. The ratio of length to the diameter of the spike to the blunt nose was varied to 6. Mair presented a report where the instability of the flow around the spike's body was observed. He explained that the flow distortion was produced due to the pressure difference between the reconnect shock at downstream and the flow inside the vortex zone. It is said that the carried-out research by Mair was the first considerable study in this field. Stalder and Nielsen (1954) were among the first researchers who investigated the aero-thermodynamic effects of the spike. They measured the heat transfer through a hemisphere-cylinder model for the Mach number between 0.12 to 5.04 ranges. Bogdonoff and Vas (1959) conducted some experimental and numerical studies on the pressure and heat transfer through a blunt nose along with a spike for a flow with the Mach number of 14. They observed that when a detached shear layer remains laminar until reaching the reconnect zone, the heat transfer through the blunt nose model diminishes significantly. Crawford (1959) performed an experimental study on a hemisphere-cylinder model to evaluate drag and aerodynamic heat transfer for the Mach number of 6.8. This experiment was operated for spikes in various lengths and the Reynolds number. In every case, the surface pressure and the heat flux of the model at the reconnect point reached a maximum value. Holden (1966) experimentally showed

that the maximum local heat transfer ratio at the reconnect point is directly proportional to the reconnect angle. In the continue, many researchers studied in terms of flow conditions (the Mach number, various Reynolds), spike's length and geometry, and different experimental configurations as parameters related to this approach (Ahmed & Qin, 2011). Dem'ianov and Shmanenkov (1960), Motoyama et al. (2001), Milicev and Pavlovic (2002), Mehta (2002), and Desai et al. (2020) showed that one could enhance the performance of spike implementation using the spiked aerodisks or hemispherical face at the tip of the spike. Furthermore, the results showed that by increasing the aerodisk diameter, the performance of aerodynamic heating deduction is improved. In addition, various studies of the aerodisk mode (flat face, hemisphere, conical), aerodisk diameter, aerodisk number, and aerodisk location on a spike have been performed (Sahoo et al., 2016; Chinnappan et al., 2017; Zhu et al., 2019; Narayana & Selvaraj, 2020; Raman et al., 2020; Sundarraj et al., 2021).

As it was explained, the counter flow jet is another approach to reducing drag. The jet output is usually placed at the stagnation point of the blunt nose. The output gas from the counter flow jet keeps the shock away from the blunt nose and leads to a decrease in the pressure dissemination on the wall (Romeo, 1963). The counter flow jets were first introduced by Eugene Love (1952) in NASA's Langly aviation laboratory in 1952 in hypersonic flow regimes and dominated the lower velocity regimes. Huang et al. (2018), numerically studied the effects of the counter flow jet on the deduction of the drag factor. Huang et al. (2018) found that when the total jet pressure falls below or exceeds the critical value, the jet goes under the long and short penetration mode, respectively. They also concluded that the performance of the total drag deduction enhanced with the total jet pressure enhancement for both long and short penetration modes. Additionally, in these studies, the total critical pressure is an essential parameter for counter flow jet design (Marley & Riggins, 2011; Shen et al., 2018). In recent years, hybrid methods such as spike and lateral jet configuration (Zhang et al., 2017; Han & Jiang, 2018; Zhu et al., 2018; Meng et al., 2021), spike and counter flow jet (Qu et al., 2018; Huang & Yao, 2019; Huang et al., 2019), counter flow jet and (Eghlima et al., 2018; Qin et al., 2018; Ou et al., 2019), and the other hybrid configurations (Ou et al., 2019; Ma et al., 2020; Ji et al., 2021; Zhu et al., 2021) have been proposed to increment the performance of drag and aerodynamic heating deduction. The study of the literature reveals that the researchers have performed widespread studies on employing various methods to improve the flow behavior and also the performance of the blunt bodies in the hypersonic flow regime. It is observed that the most of studies are focused on the effectiveness of one of these approaches and have studied that special one from different points of view. However, in terms of implementing various control methods and their effectiveness evaluation with a constant flow condition and a constant geometry, no research has been carried out. Researchers have conducted extensive studies on the use of various methods to improve the flow behavior and performance of a blunt nose in hypersonic flow regimes.

Therefore, as stated in the literature and mentioned in the introduction of the article, most studies have focused on the effectiveness of a specific flow control approach and examined its effects. However, the implementation of different control methods and evaluating the effectiveness of different methods in a fixed geometry (blunt nose) and under similar flow conditions has not been studied. Therefore, the present study aims to investigate the effects of different control methods on flow behavior, drag deduction, and aerodynamic heating. Accordingly, in this research, the effects of seven various control configurations on the flow behavior around a constant blunt nose in the Mach number of 6 are studied, and the effects of these configurations are detachedly and numerically studied on the flow behavior, drag, and heating factors of the blunt nose.

In the continue, the following subjects are investigated. In part 2, the governing equations are presented. Part 3 discusses validation, numerical method, and mesh independence in detail. In part 4, the effectiveness of the various configurations and their model and dimensions are studied. Part 5 presents the numerical results and explains how every seven configurations affect the flow characteristics, and also presents the performance of drag factor deduction and heat flux. Eventually, the output results are shown in part 6.

2. GOVERNING EQUATIONS

The Reynolds-averaged Navier-Stokes (RANS) equations are solved using the finite volume method (FVM), which discretizes the computational domain into a grid of control volumes. The boundary conditions, steady-state assumptions, and density-based solvers are considered for the simulation analysis. The continuity equation ensures mass conservation, the momentum equation accounts for the conservation of momentum, and the energy equation captures the conservation of energy. The ideal gas law is also incorporated to relate pressure, density, and temperature.

By solving these equations numerically, it is possible to analyze the behavior of compressible axisymmetric supersonic flows over a conical nose. The simulation enables the investigation of various flow properties, including velocity, pressure, density, and temperature disseminations, providing insights into the aerodynamic characteristics of the system.

Continuity equation:

$$\frac{\partial \rho}{\partial t} + \frac{\partial \rho u_i}{\partial x_i} = 0 \tag{1}$$

Momentum equation:

$$\frac{\partial (\rho u_i)}{\partial t} + \frac{\partial \rho u_i u_j}{\partial x_j} = -\frac{\partial P}{\partial x_i} + \frac{\partial \tau_{ij}}{\partial x_j} \tag{2}$$

Energy equation:

$$\frac{\partial (\rho E)}{\partial t} + \frac{\partial \rho H u_j}{\partial x_j} = \frac{\partial}{\partial x_j}\left(u_i \tau_{ij}\right) - \frac{\partial}{\partial x_j}\left(\left(\frac{\mu_l}{Pr} + \frac{\mu_t}{Pr_t}\right)\frac{\partial T}{\partial x_j}\right) \tag{3}$$

Equation 4 represents the viscous stress tensor τij, which is related to the velocity gradients and viscosity

factors. Equation 5 represents the strain rate tensor s_ij, which describes the deformation of the fluid flow. In these equations, ρ represents the density, u_i represents the velocity component in the xi direction, p represents the pressure, and T represents the temperature. The factors μl and μt represent the laminar and turbulent viscosity factors, respectively.

$$\tau_{ij} = 2(\mu_l + \mu_t)\left(s_{ij} - \frac{1}{3}s_{kk}\delta_{ij}\right) \tag{4}$$

$$s_{ij} = \frac{1}{2}\left(\frac{\partial u_i}{\partial x_j} + \frac{\partial u_j}{\partial x_i}\right) \tag{5}$$

The gas pressure P is obtained from the perfect gas equation (Equation 6):

$$P = \rho RT = (\gamma - 1)\left[\rho E - \rho k - \frac{1}{2}\rho(u^2 + v^2 + w^2)\right] \tag{6}$$

Equation 7 defines the total energy (E) and Equation 8 defines the total enthalpy (H). In these equations, R represents the gas constant, γ represents the specific heat ratio (with a constant value of 1.4), and k represents the turbulent kinetic energy. The total energy (E) is given by a combination of the kinetic energy and internal energy, while the total enthalpy (H) includes the contribution of pressure.

$$E = e + k + \frac{1}{2}(u^2 + v^2 + w^2) \tag{7}$$

$$H = h + k + \frac{1}{2}(u^2 + v^2 + w^2) \tag{8}$$

Where e and h represent the internal energy and enthalpy, respectively, and are related to each other through equation 9.

$$h = e + \frac{P}{\rho} \tag{9}$$

To model the turbulence of the flow, and consider the high Reynolds number of the flow, the k-ω SST turbulence model has been used in many studies and has shown high accuracy (Menter, 1994). In this study, this turbulence model is also used (equations 10 and 11):

$$\frac{\partial \rho k}{\partial t} + \frac{\partial(\rho u_j k)}{\partial x_j} = P_k - \beta^* \rho \omega k + \frac{\partial}{\partial x_j}\left[(\mu_L + \mu_T \partial_k)\frac{\partial k}{\partial x_j}\right] \tag{10}$$

$$\frac{\partial \rho \omega}{\partial t} + \frac{\partial(\rho u_j \omega)}{\partial x_j} = \frac{\gamma}{\mu_T}P - \beta \rho \omega^2 + 2(1 - f_1)\frac{\rho \sigma_{\omega 2}}{\omega}\frac{\partial k}{\partial x_j}\frac{\partial \omega}{\partial x_j} + \frac{\partial}{\partial x_j}\left[(\mu_L + \sigma_\omega \mu_T)\frac{\partial \omega}{\partial x_j}\right] \tag{11}$$

Where k represents the turbulent kinetic energy, and ω represents the specific dissipation rate.

Also, the energy equation in this study is solved as follows (Bhamare et al., 2020):

$$\frac{\partial}{\partial t}(\rho E) + \nabla.\left(k_{eff}\nabla T - \sum_j h_j \vec{J}_j + \left(\bar{\bar{\tau}}_{eff}.\vec{\vartheta}\right)\right) + S_h \tag{12}$$

Where K_{eff} represents the effective conductivity, which is the sum of the thermal conductivity (k) and the turbulent thermal conductivity (k_t) based on the selected turbulence model. $\vec{J}_j$ Denotes the diffusion flux of species j. The terms on the right-hand side of Equation (12) correspond to energy transfer resulting from conduction, species diffusion, and viscous dissipation. S_h incorporates the heat of chemical reaction and any other volumetric

heat sources specified. In Equation (12), E is defined as follows.

E in equation (12) is defined as follows

$$E = h - \frac{p}{\rho} + \frac{\vartheta^2}{2} \tag{13}$$

Where sensible enthalpy h is defined for ideal gases as

$$h = \sum_j Y_j h_j \tag{14}$$

In Equations (12) and (14), Y_j is the mass fraction of species j and h_j is as follows

$$h_j = \int_{T_{ref}}^{T} c_{p.j} \, dT \tag{15}$$

Where T_{ref} is 298.15 K.

3. NUMERICAL VALIDATION

3.1 FIRST VALIDATION MODEL

The geometrical model has been validated in order to prove the accuracy of calculations from the aspect of aerodynamic heating in the presence of the counter flow jet. Of course, it should be mentioned that the more important aspect of this validation is the validation of numerical data compared to the results obtained in the real world, which are found in experimental studies. This geometric model is derived from the experimental study of Hayashi et al (Hayashi et al., 2006). The geometric model to be validated is a blunt nose. In front of the nose of this geometric model, a sonic nozzle is placed in order to blow a counter flow jet against the free flow. According to the information presented in the article by Hayashi et al. (Hayashi et al., 2006), the diameter of the blunt nose is 50 mm, the diameter of the sonic nozzle is 4 mm, the free flow Mach number is 3.98, and the jet Mach number is 1. In their study, Hayashi and his colleagues used a typical supersonic wind tunnel at Kyushu University to obtain the free-flow Mach number. Also, in his experimental study, Hayashi investigated four different total pressure ratios of 0.2, 0.4, 0.6, and 0.8 respectively. But in this section, we only measure the total pressure ratio of 0.4. In the simulation, the Stanton number is used to present the heat flux and defined as follows (Hayashi et al., 2006).

$$St = \frac{q_w}{(T_{aw} - T_W)\rho_\infty c_{p,\infty} V_\infty} \tag{16}$$

$$T_{aw} = T_\infty \left\{ 1 + \sqrt[3]{Pr_w} \left[\frac{\gamma - 1}{2} \right] Ma_\infty^2 \right\} \tag{17}$$

Where q_w is the surface heat flux, T_{aw} is the adiabatic wall temperature and T_w is the wall temperature. ρ_∞, V_∞ and M_∞ are the free stream density, velocity, and Mach number, respectively. $\gamma = 1.4$ is the ratio of specific heat.

In this study, Hayashi and his colleagues (Hayashi et al., 2006) mentioned that heat flux measurements in this article are based on calorimetric techniques. The diameter and length of the calorimeter are 2 and 5 millimeters, respectively. The calorimeter temperature is measured by thermocouples connected to the bottom of the calorimeter. Several calorimeter sensors are installed in the blunt nose. The measurement points range from an angle θ of 20

degrees to 90 degrees, where θ is the angle measured from the central axis of the geometric model. Therefore, in the numerical analysis performed in this article, 9 points on the blunt nose were selected at angles from 10 to 90 degrees. At these 9 points, the Stanton number values were extracted as the accuracy parameter for estimating the CFD solution in the ANSYS-FLUENT software. The calculated Stanton numbers at these 9 points were compared with the values extracted from the empirical and numerical models calculated by Hayashi and colleagues (Hayashi et al., 2006). The maximum relative error compared to the experimental results is 1.95%, which is acceptable.

As shown in Fig. 1, the contour of the density gradient obtained from the numerical solution is very similar to the Schlieren image obtained from the experimental study of Hayashi et al (Hayashi et al., 2006). In addition, the comparison between the Stanton number obtained from the numerical solution and the experimental data of reference (Hayashi et al., 2006) is shown in Fig. 2. As it is known, the Stanton number calculated in this paper clearly predicts the process of heat flux changes along the surface, and the current prediction is better than the prediction in reference (Hayashi et al., 2005) which was numerically investigated by Hayashi et al. As a result, the numerical solver used in the present study is suitable for a complex flow field investigation when there are different hybrid configurations. Also, the proof of this numerical solution shows that the numerical solution results of the presented configurations can be used in reality.
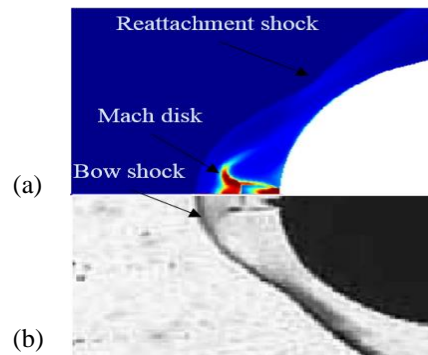

Fig. 1 Comparison of the density contour (a) with the available experimental image (b) (Hayashi et al., 2006)
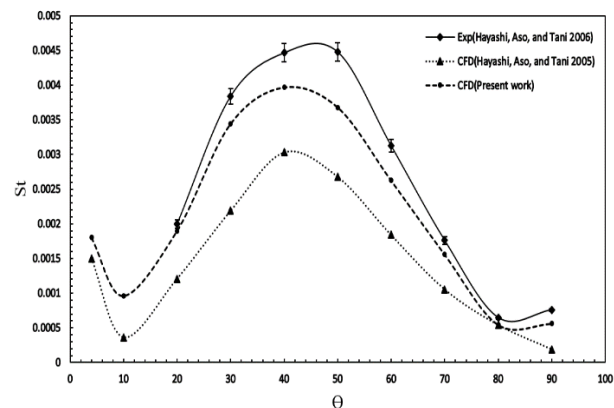

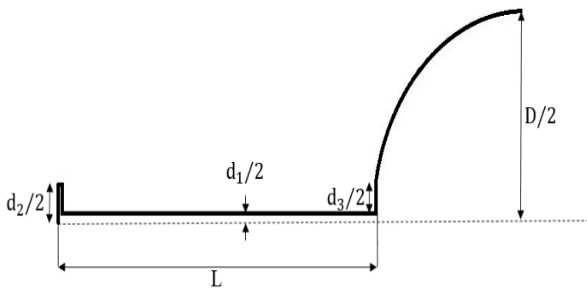**Fig. 2 Comparison of Stanton number dissemination of blunt bodies**

Fig. 3 Schematic of the geometric validation model ([Vali & Abbasi, 2022](#))

Table 1 Dimensions of the geometric model ([Vali & Abbasi, 2022](#))

L (mm)	D (mm)	d_1 (mm)	d_2 (mm)	d_3 (mm)
100	100	4	16	2

3.2 Second Validation Model

In this study, the validation and grid independence of the mesh results were examined. As the authors have already addressed the validation and grid independence of the mesh results in reference ([Vali & Abbasi, 2022](#)), these findings are not reiterated in this article to avoid redundancy. For details on the grid independency from the mesh and validation, refer to reference ([Vali & Abbasi, 2022](#)). It should be noted that all the conditions used in the numerical solution of this configuration, including the flow conditions, boundary conditions, and solution settings, were used in other parametric settings of this article. (This paragraph refers to Fig. 3 and Table.1.)

4. PARAMETRIC STUDY OF SEVEN GEOMETRICAL MODELS

In the current research, the aim is to study seven various geometrical configurations in order to investigate the effect of each configuration on drag and aerodynamic heating and select the best one in terms of drag and aerodynamic heating improvement. For this purpose, according to Fig. 4, seven different configurations are analyzed, which include: (a) blunt nose configuration, (b) blunt nose with a spike, (c) blunt nose with an counter flow jet, (d) blunt nose with a spike and root counter flow jet, (e) blunt nose with a spike and aerodisk, (f) blunt nose with a spike, aerodisk and root counter flow jet, (g) blunt nose with a spike, four aerodisks and root counter flow jet. Furthermore, to evaluate the results, the output parameters such as drag and aerodynamic heating factors for each geometrical model of (b) to (g) are compared with the blunt nose geometrical model of (a) (as a reference). The parameters and dimensions of each mentioned configuration are shown in Fig. 4 and Table 2. The nose form is the same in every configuration. Also, the presented value dimensions in Fig. 4 and Table 2 are

illustrated as abbreviation symbols. Where t is the thickness of the flat face disk, Lf is the length of conical aerodisk, δ is the nose angle of conical aerodisk with vertical axis, L is the spike length, d_2 is the spike diameter, D is the blunt nose diameter, d_3 is the flat face aerodisk, and d_4 is the output jet diameter.

Also, in order to present the general pattern of the flow and phenomena occurring in the hypersonic flow around the blunt nose, a schematic of 7 geometric models is presented in Fig. 5. It is known that the flow recorded in 7 configurations is very complex, and includes various types of shock waves including bow shock wave, oblique shock wave, detached shock wave, reconnect shock wave and shock-shock interaction. Of course, in order to extract detailed information about the flow structure in these configurations, the results are presented in detail in the rest of the article.

Also, in order to present the general pattern of the flow and phenomena occurring in the hypersonic flow around the blunt nose, a schematic of 7 geometric models is presented in Fig. 5. It is known that the flow recorded in 7 configurations is very complex, which includes various types of shock waves including bow shock wave, oblique shock wave, detached shock wave, reconnect shock wave and shock-shock interaction. Of course, in order to extract detailed information about the flow structure in these configurations, the results are presented in detail in the rest of the article.

4.1 Numerical Model

In this study, the geometry of the blunt nose and the flow conditions are similar to the previous geometry in Reference ([Vali & Abbasi, 2022](#)). Therefore, based on these boundary conditions, the turbulence model and the solution methods considered for seven configurations are similar to the previous model in Reference ([Vali & Abbasi, 2022](#)).

The boundary conditions used for seven geometrical models are the same and as follows: for free flow Mach number (Ma_∞) 6, static pressure (P_∞) 21.96 Pa, static temperature (T_∞) 247.02 K, Reynolds number is 4×10^5 and angle of attack (α) is zero. The boundary condition for all walls is assumed to be non-slip and isothermal with a temperature of 300 K. Also, the value of turbulent viscosity ratio at the inlet and outlet is considered to be 10% and the intensity of the inlet turbulence is considered to be 2%. In this paper, drag force and aerodynamic heating are calculated by solving the Reynolds Averaged Navier-Stokes (RANS) equations. Turbulence model *SST* $k- \omega$ is used due to considering the flow near the wall, especially in the presence of reverse pressure gradient, it performs a better and more accurate simulation.

Also, for the configurations where the counter flowing root jet is employed, the parameters are as below:

Table 2 Dimension values of the geometrical model

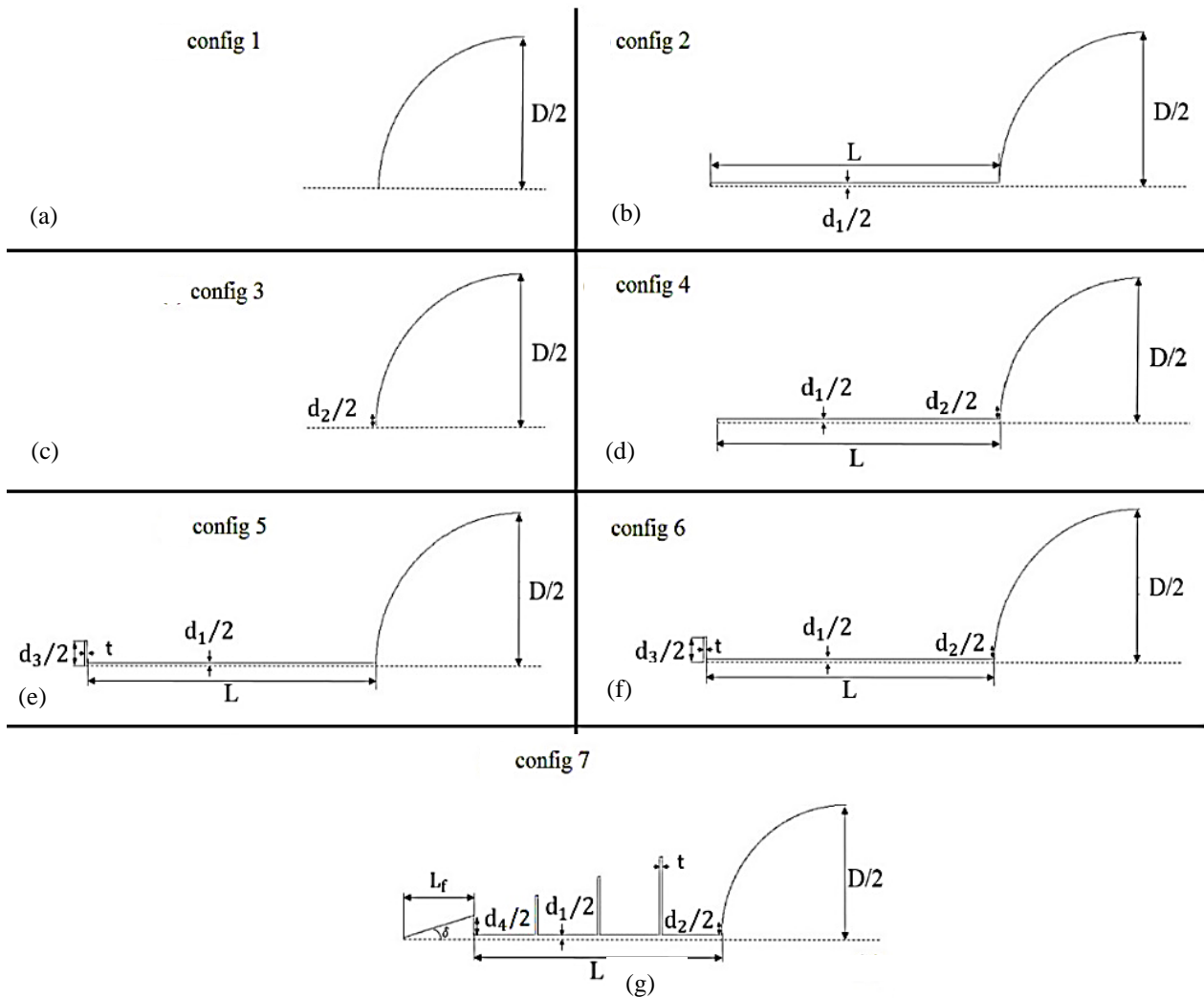| Lf (mm)	δ (deg)	L (mm)	D (mm)	d_4 (mm)	d_3 (mm)	d_2 (mm)	d_1 (mm)	t (mm)
28.5	17	100	100	14	16	4	2	1

Fig. 4 Dimensions of the geometrical models

The Mach number of the counter flow jet (Ma_{jet}) equals 1.5, the total pressure of the counter flow jet (P_{0jet}) is 6934 Pa, and the total temperature of the counter flow jet (T_{0jet}) equals 300 K. The ratio of the counter flow jet's total pressure: (PR), the ratio of counter flow jet's total pressure(P_{0jet}), and the total pressure of the free stream(P_∞). The ratio of the counter flow jet's total pressure ratio is 0.2. The flow is freestream, and the jet is countered to the perfect gas flow. The perfect gas utilized in the counter flowing root jet, and freestream was air.

According to Fig. 6, the relative changes in specific heat ratio with respect to temperature within the desired temperature range (300 to 2000 Kelvin) in this study are very negligible. Accordingly, these parameter variations do not have a significant influence on the present problem. Despite this fact, in order to obtain accurate results, the variations in specific heat ratio with respect to temperature within the provided range in Fig. 6 have been considered in the Fluent software.

In this paper, drag force and aerodynamic heating are calculated by solving the Reynolds Averaged Navier-Stokes (RANS) equations. Turbulence model $SST\ k-\omega$ is used due to considering the flow near the wall, especially in the presence of reverse pressure gradient, it performs a better and more accurate simulation.

In Fig. 7, the boundary conditions and the computational meshing are illustrated for seven presented configurations. As it is obvious, the accuracy of the numerical solution result is greatly influenced by the quality of the meshing. Therefore, in all configurations, the computational domain is divided into several layers to ensure high meshing quality near the wall where severe aerodynamic and thermal changes occur. Also, the height of the first mesh layer next to the wall is 1×10^{-6} m to ensure the dimensionless parameter y+ <1 near the wall.

The current simulation was performed using the commercial software ANSYS-Fluent 2020. The effectiveness of this commercial software in terms of credibility and accuracy has been demonstrated in numerous research studies and articles. In the present study, a model presented in a previous article was considered, and the results obtained from the flow analysis with the software were compared to the results of the reference article, showing an acceptable level of accuracy. The independence of the results from the grid size was investigated, and the results were presented in a previous article by (Vali & Abbasi, 2022), to which reference has been made for brevity.

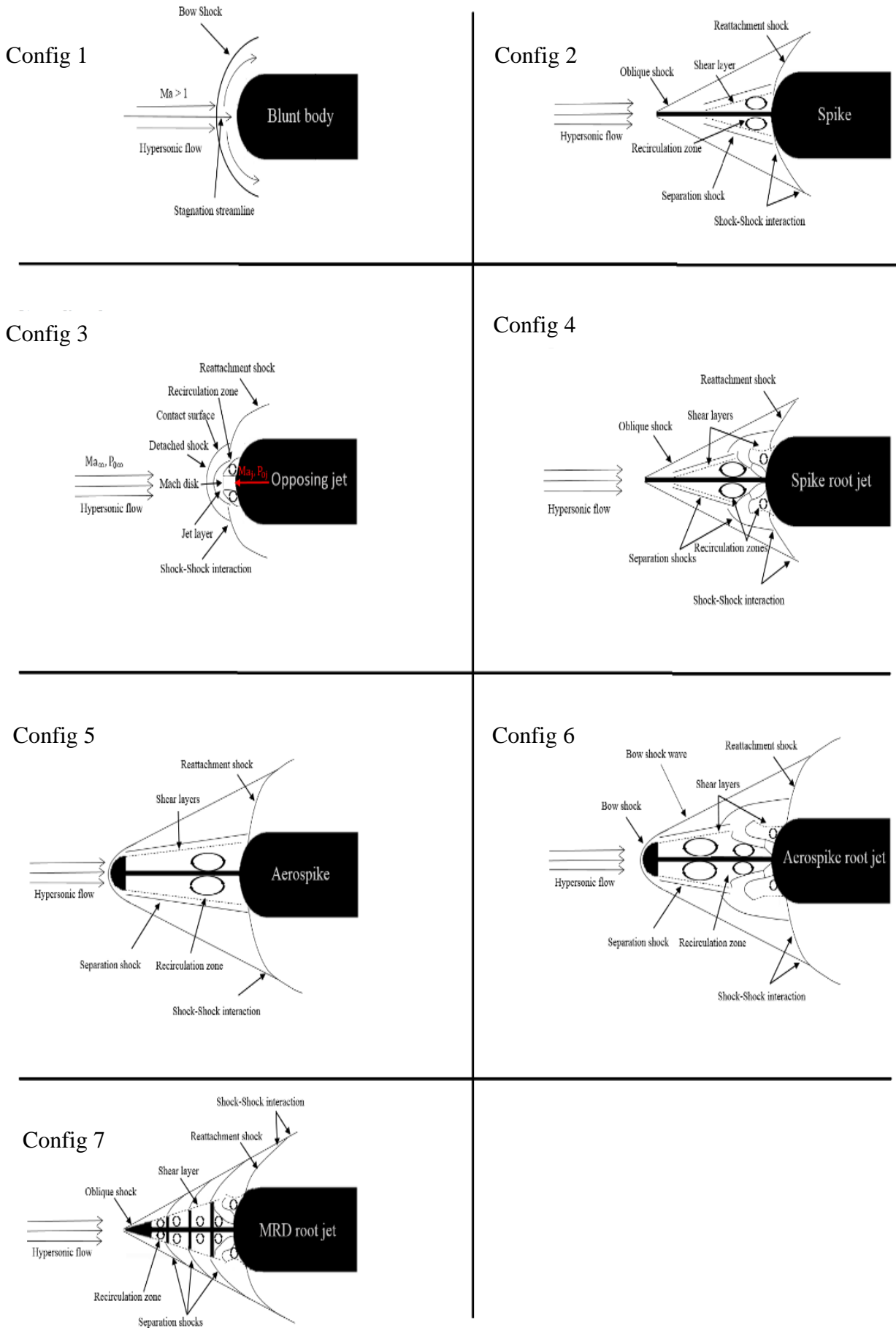Various aspects of performance in this simulation have been addressed, including the use of a second-order

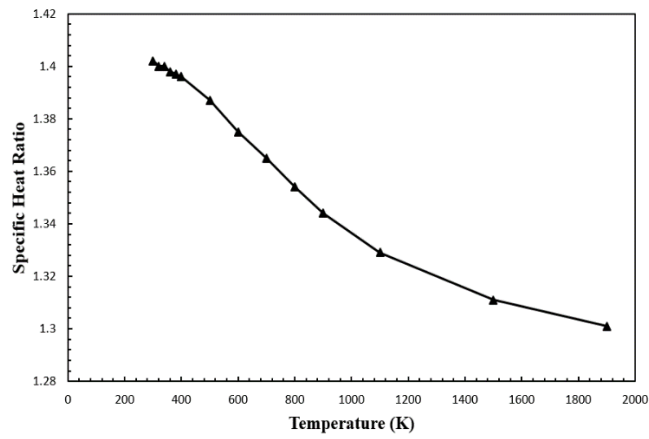**Fig. 5 Schematic of flow structure for 7 configurations**

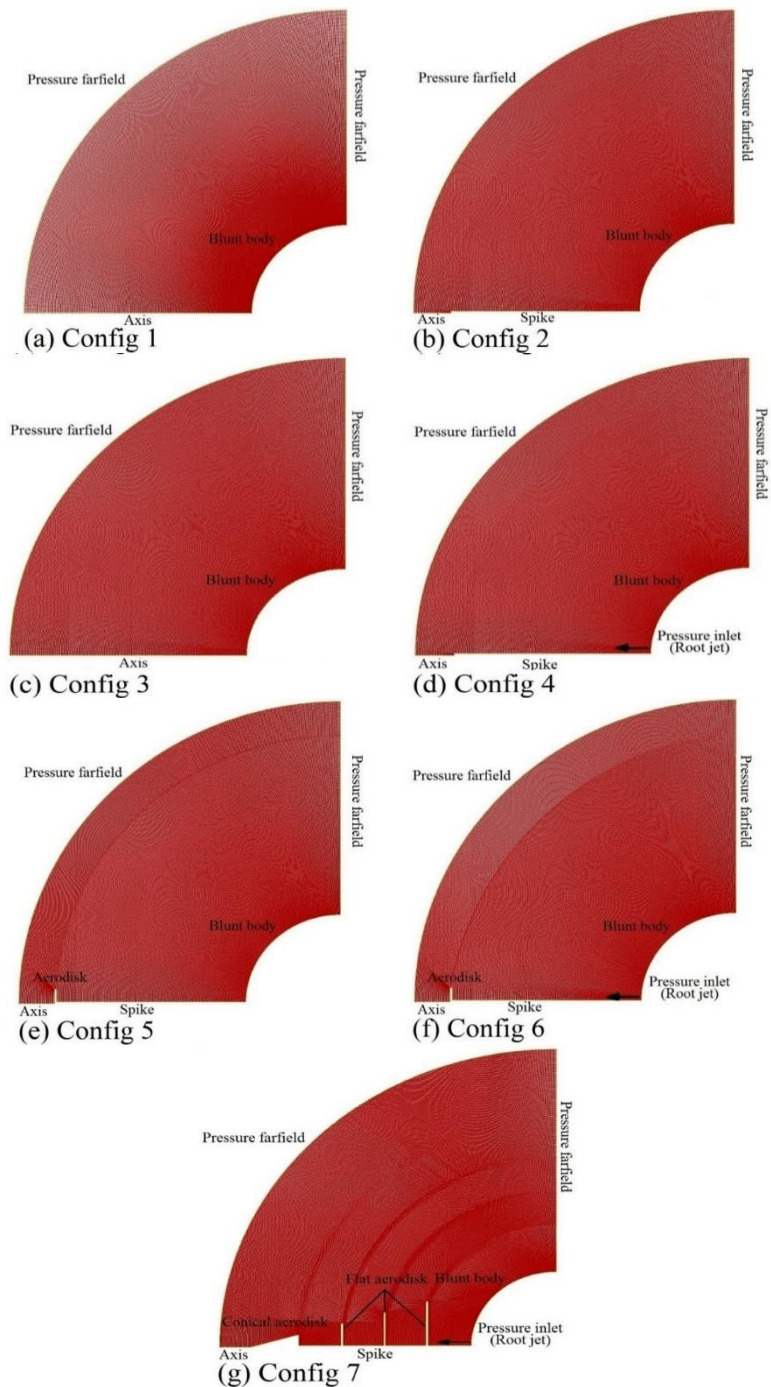**Fig. 6 Value of specific heat ratio (g) in terms of temperature**

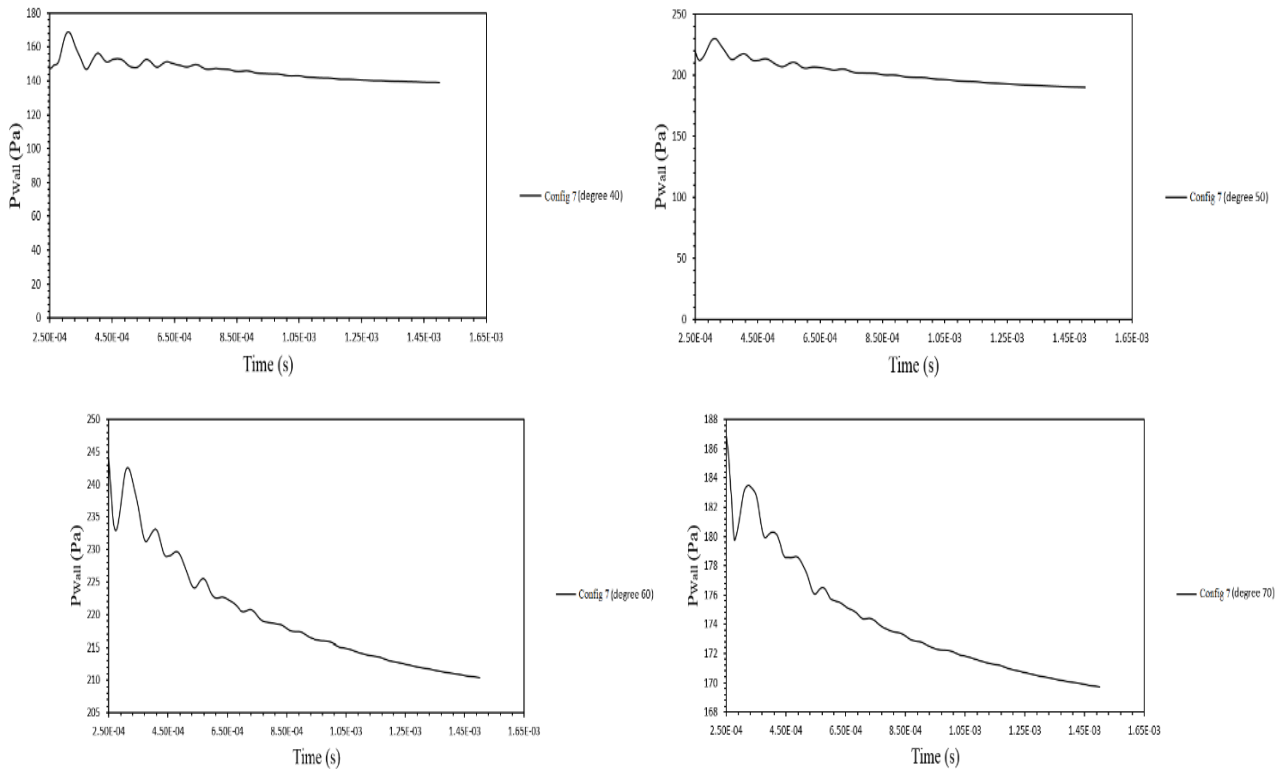**Fig. 7 Boundary conditions and meshing of seven geometrical models**

Fig. 8 Pressure fluctuations at four different theta angles for configuration 7

discretization scheme to enhance the numerical solution accuracy. In the solution methodology, the lower-upper symmetric Gauss-Seidel implicit scheme method (LU-SGS) was utilized for temporal discretization, and the Courant-Friedrichs-Lewy (CFL) number was set to 5.

Also, investigation of various studies (Yamauchi et al., 1995; Guenther & Reding, 1977; Ahmed & Qin, 2014; Betelin et al., 2018; Kushnirenko et al., 2021) shows that two-dimensional axisymmetric flow analysis provides accurate and acceptable results.

Furthermore, the validation of the results in the present study (which has been performed in a two-dimensional axisymmetric manner) confirms this issue in comparison with experimental results (Sahoo et al., 2016, 2019).

Regarding the point raised by the esteemed reviewer, which mentions the possibility of initially symmetric flow conditions leading to flow oscillations over time, the authors have conducted a transient analysis for Configuration 7. The results of this transient analysis indicate that no flow oscillations occur in the current model over time, and the flow conditions remain unchanged. As shown in Fig. 8, the pressure oscillation conditions at theta angles of 40, 50, 60, and 70 degrees, where the greatest pressure effects occur, have been extracted in the transient analysis conditions.

5. RESULTS AND DISCUSSION

In this section, seven proposed configurations are studied and the output results are compared with each other. The flow characteristics and the effectiveness of each configuration on drag and aerodynamic heating are

evaluated. Regarding the constant geometrical form of the nose in every configuration, the comparison of the results for each configuration is performed using only the nose state, and the effects of applying different control methods are evaluated.

In Figs 9 and 10, the Mach number contours and the temperature are shown for seven configurations. Figure 9 shows the obtained Mach contours and flow contours as results of the numerical solution of seven geometrical models with different configurations. Configuration 1 shows the primary geometry (blunt nose). In this configuration, the bow shock is generated in front of the nose, which is a detached compression forward wave and is a combination of normal shock and infinite oblique shocks. The bow shock produces an intense normal shock inside the stagnation zone of the nose, which leads to the formation of aerodynamic heating and a great drag on the nose. In configuration 2 (blunt nose with a spike), a bow shock is generated on the spike's tip, which leads to a significant increment in the pressure and temperature on the spike's tip.

The compressed flow is diffused by the bow shock along the spike and the flow detached occurs in the downstream. Thus, the shear layer, vortex zones, and detached shock are produced. In configuration 3 (the blunt nose and counter flow jet geometrical models), it is observed that the counter flow jet collides with and is compressed by the free stream and is shaped as a Mach disk in front of the nozzle. Afterward, the gas fluid is returned to the nose's walls, and a vortex zone is formed in front of the nose. Consequently, the growing shear layer flows along the blunt nose to the downstream and collides with the blunt nose walls. As a result, a reconnect shock is created on the blunt nose edge. Also, similar to configuration
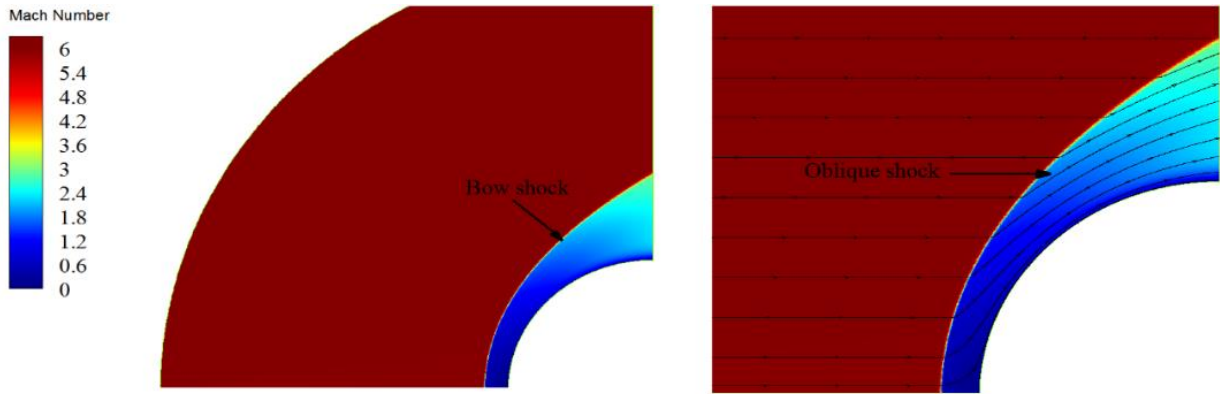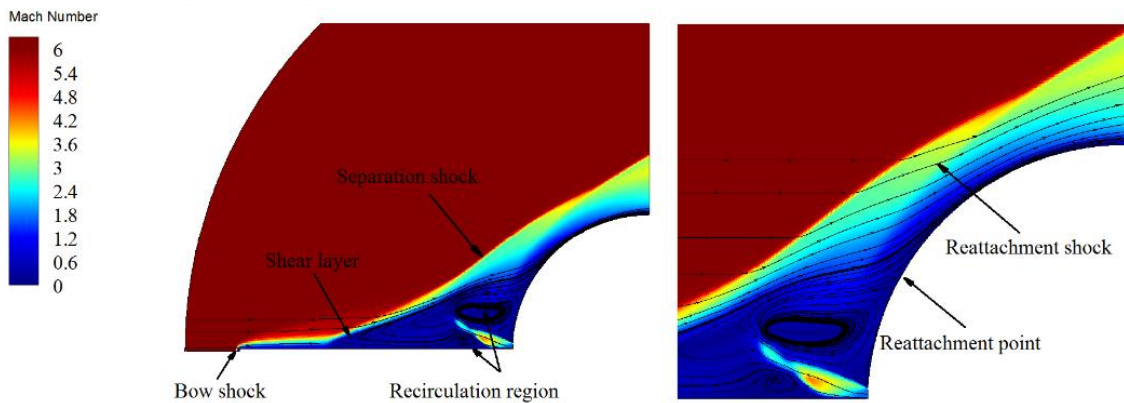
(a) Config 1
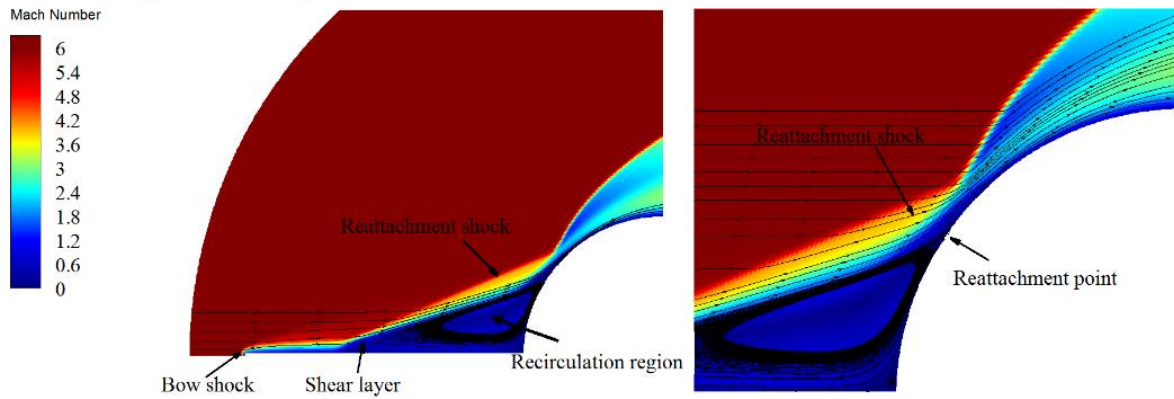
(b) Config 2
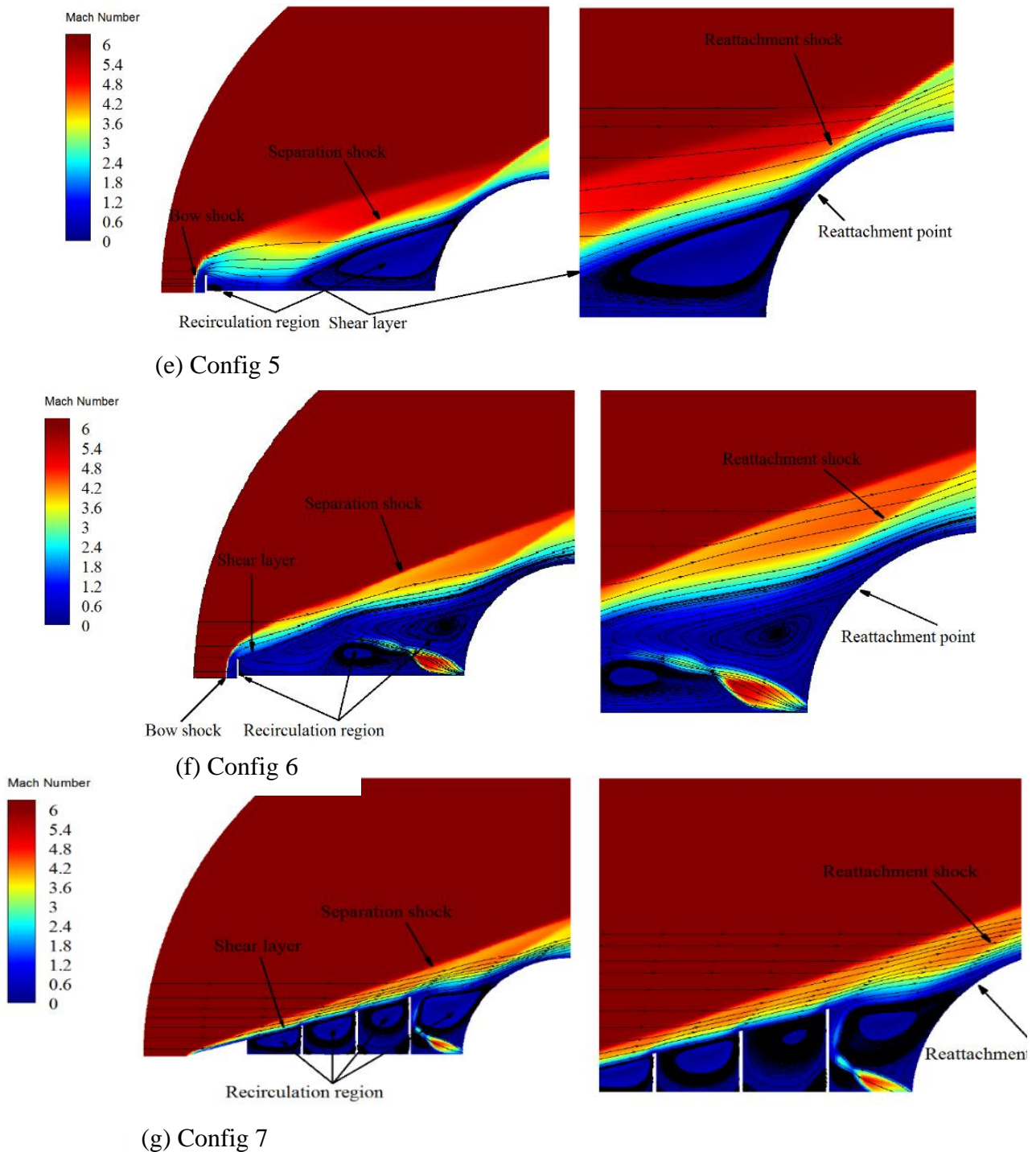

(c) Config 3
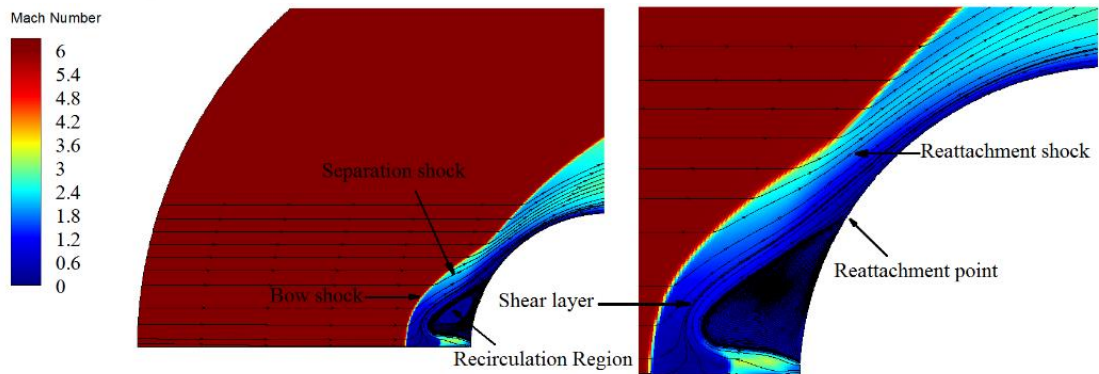
(d) Config 4

(e) Config 5

(f) Config 6

(g) Config 7

Fig. 9 Mach contours of the seven geometrical models

2, the detached shock interferes with the reconnect shock, and the shock-shock interaction occurs. Configuration 4 (blunt nose, spike and counter flow jet) is a kind of combination of configurations 2 and 3. The flow behavior, in this case, is similar to case 2 with difference which is that employing the counter flowing root jet guides the growing shear layer to the upper levels, and collides with the blunt nose, and a reconnect shock is generated on the blunt nose edge as a consequence. Moreover, compared with the case without counter flowing root jet, the reconnect shock gets closer to the blunt nose edge. In configuration 5 (spike and aerodisk configuration), the

aerodisk compresses the hypersonic free stream in front of itself to convert it to the bow shock. Aerodisk compresses the free stream using the spike and diminishes the gas velocity when it flows to reach the nose. Furthermore, a greater vortex zone is formed in front of the nose. In this configuration, a reconnect shock is generated on the nose's edge, similar to other configurations. Additionally, in this configuration, the reconnect shock interacts with detached shock likewise. In configuration 6 (geometry model of spike, aerodisk and counter flow jet), it is observed that the flow field gets more complicated due to a root jet. As the figure shows, the vortex zone is divided
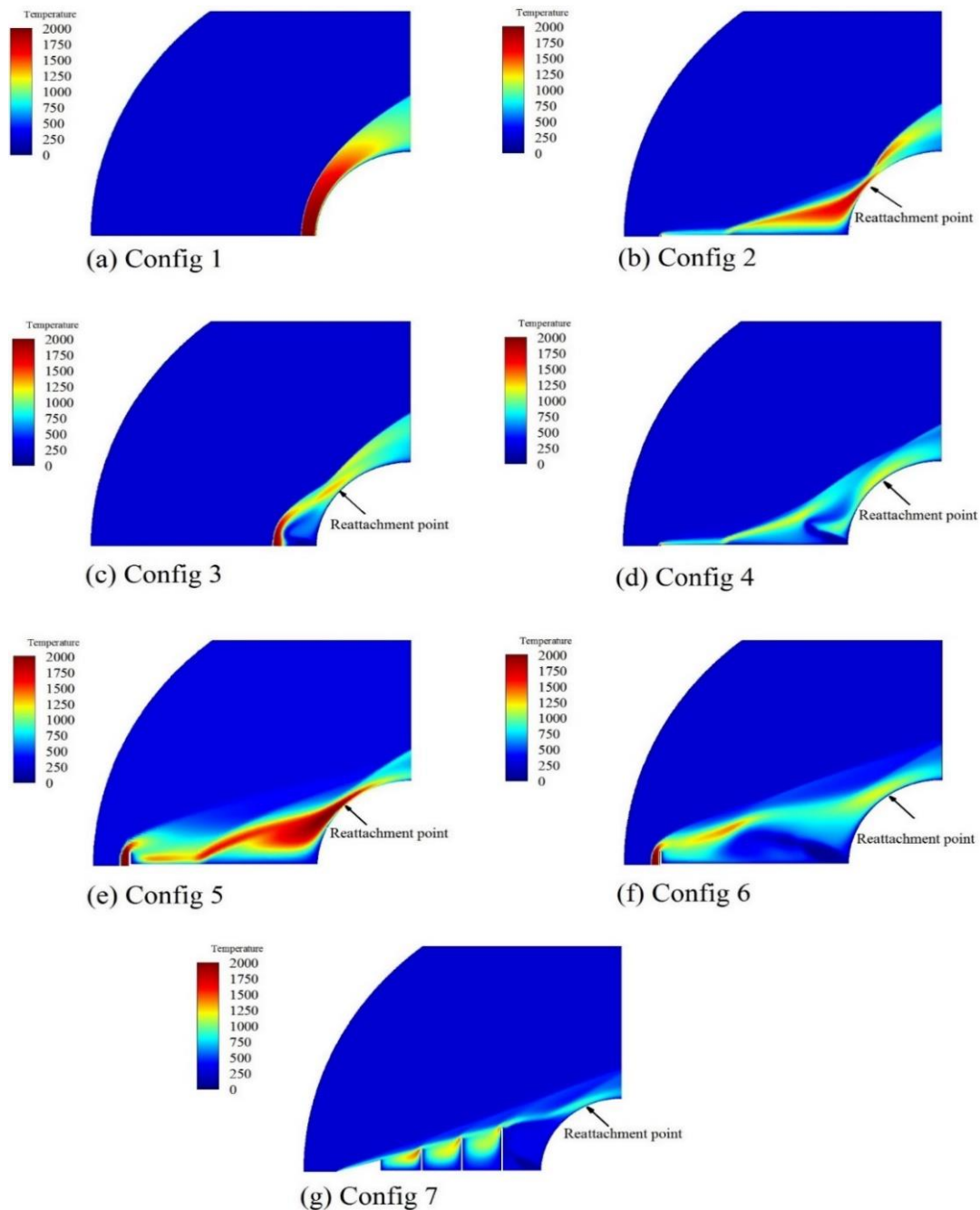
Fig. 10 Static temperature contour of the seven geometrical models

into three regions by the high-pressure output jet gas. Secondly, the counter flow jet pushes the shear layer to the upper level, which weakens the reconnect shock intensity and diminishes the pressure along the blunt nose. Also, the shock-shock interaction occurs at a distance very farther than the nose, so the shock-shock interaction could be neglected due to no effect on the nose. In configuration 7 (geometrical model of the spike, four aerodisks, and counter flow jet), the conical aerodisk converts the main bow shock into the oblique shock. This leads to flow detached and the formation of low-pressure vortex zones along the spike and in front of the blunt nose.

Furthermore, the shear layer, vortex zones, and detached shock are generated. In the continue, the growing shear layer collides with the flat face aerodisks, which leads to the shear layer rising. Then, the pressure of the output jet results in higher penetration to the shear layer and colliding the shear layer to a location close to the blunt nose edge. This leads to forming a longer weak vortex zone in length and width in front of the blunt nose and close to its walls. Also, this results in collision of the reconnect shock with the blunt nose at a farther distance. Moreover, the reconnect shock's intensity gets highly diminished, and the shock-shock interaction disappears.

In Fig. 10, the static temperature contours obtained by the numerical solution of the seven different geometrical configurations are shown. According to configuration 1 (blunt nose), due to the bow shock presence in front of the nose, the maximum temperature is applied to the nose inside the stagnation zone. With going away from the stagnation zone, the normal shock converts into the oblique shock, and the heat transfer gets diminished. In

configuration 2 (blunt nose and spike), because of the spike presence, the bow shock gets converted to the oblique shock, and flow detached occurs. This leads to the formation of a low-temperature weak vortex zone close to the nose. However, since the stagnation zone is inside the vortex zone, the gas temperature gets lower close to the stagnation zone, and this leads to a deduction in heat transfer through the nose's walls. Furthermore, since the reconnect shock has less intensity, the temperature is decreased inside the reconnect shock zone. In configuration 3 (blunt nose and counter flow jet), the counter flow jet generates a vortex zone attached to the walls of the blunt nose. Nonetheless, regarding the fact that the stagnation zone is inside the fluid inlet section, the low temperature counter flow jet and the vortex zone result in a temperature drop in this region, and the temperature of the gas near the stagnation point is decreased. This leads to a deduction in heat transfer through the blunt nose walls. Also, the temperature drops due to a decrease in the reconnect shock. In configuration 4 (blunt nose, spike, and counter flow jet), the presence of the spike leads to flow detached and produces a vortex zone inside the stagnation region attached to the nose's walls. Additionally, the counter flowing root jet injects the low-temperature fluid into the vortex zone, which makes the vortex zone larger along the spike. Although, because the stagnation region and the counter flowing get are inside this zone, the gas temperature close to the stagnation zone gets lower which leads to lower heat transfer through the walls of the nose. On the other hand, since the reconnect shock has less intensity, the temperature in this zone is also diminished. In configuration 5 (blunt nose, spike, and aerodisk), the aerodisk causes the hypersonic free stream to be compressed in front of itself in order to create the bow

shock in front of the spike and itself. Aerodisk, along with the spike, compresses the free stream and diminishes the gas velocity reaching the nose, and also decreases the reconnect shock intensity. Moreover, due to the presence of the aerodisk, a larger and lower temperature vortex zone is produced compared to configuration 2. In configuration 6 (blunt nose, spike, aerodisk and counter flow jet), due to the counter flow jet presence, the low-temperature output gas generated by the counter flow jet penetrates the hypersonic free stream. This low-temperature gas keeps the reconnect shock away from the blunt nose and decreases the reconnect shock's intensity. Thanks to the presence of the spike, and counter flow jet inside the stagnation zone, and the intensity deduction of the reconnect shock, the temperature in the reconnect point and on the blunt-body is decreased in total. In configuration 7 (blunt nose, spike, four aerodisks and counter flow jet), aerodisks diminish the intensity of the oblique and reconnect shocks. On the other hand, low-pressure and temperature vortex zones tend to grow larger due to the aerodisk existence. The overall mentioned events diminish the temperature applied on the blunt nose walls and the reconnect point.

Figure 11 shows the comparison of the total drag factor of the whole configuration. Also, the amount of generated drag factor on each element, such as the spike, blunt nose, and aerodisk, are mentioned.

Additionally, regarding Fig. 11, the amount of applied drag factor to the spike and aerodisks to the total drag factor for configurations 2, 4, 5, 6, and 7 are %28, %17, %7.31, %11.2, and %11.5 respectively which have a negligible effect on the total applied drag factor on the whole geometrical body.

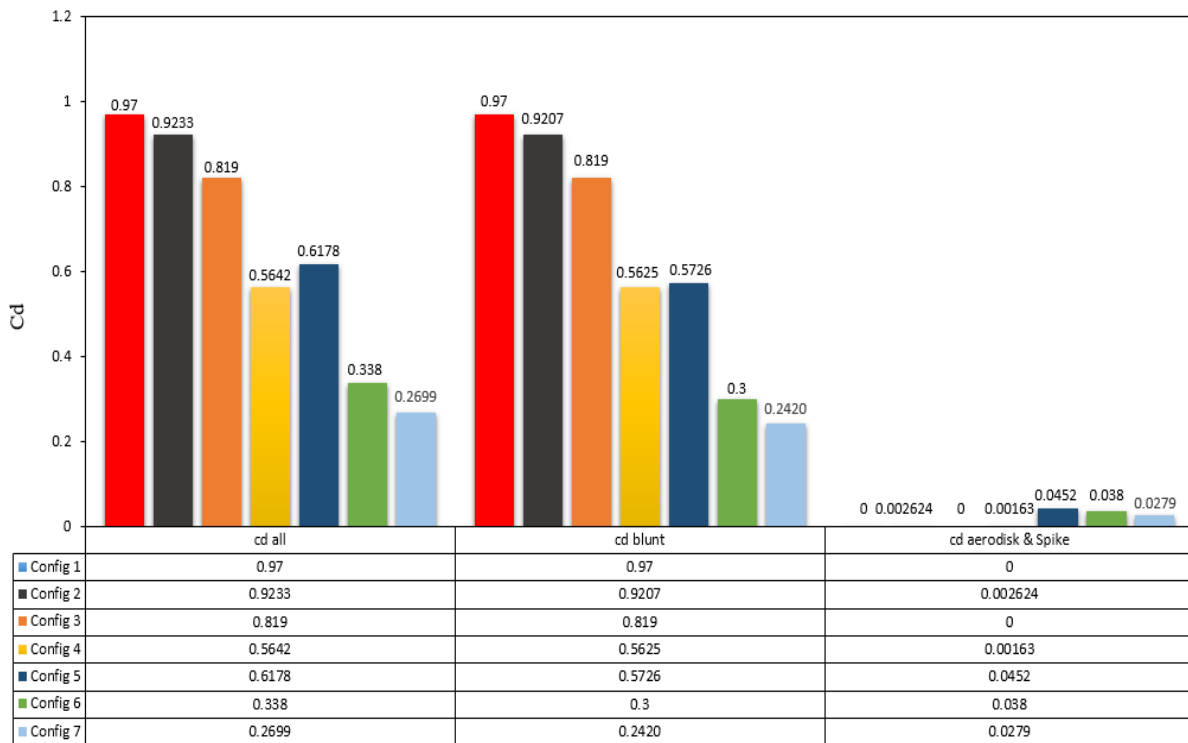|	cd all	cd blunt	cd aerodisk & Spike
Config 1	0.97	0.97	0
Config 2	0.9233	0.9207	0.002624
Config 3	0.819	0.819	0
Config 4	0.5642	0.5625	0.00163
Config 5	0.6178	0.5726	0.0452
Config 6	0.338	0.3	0.038
Config 7	0.2699	0.2420	0.0279

Fig. 11 Comparison of the total drag factor on seven configurations

Table 3 Performance of drag factor deduction for each of the configurations to configuration 1

Model	Config 2	Config 3	Config 4	Config 5	Config 6	Config 7
K	4.8%	15.5%	41.8%	36.3%	65.1%	72.1%

Table 4 Performance of the total drag factor deduction for configuration 7 to other configurations

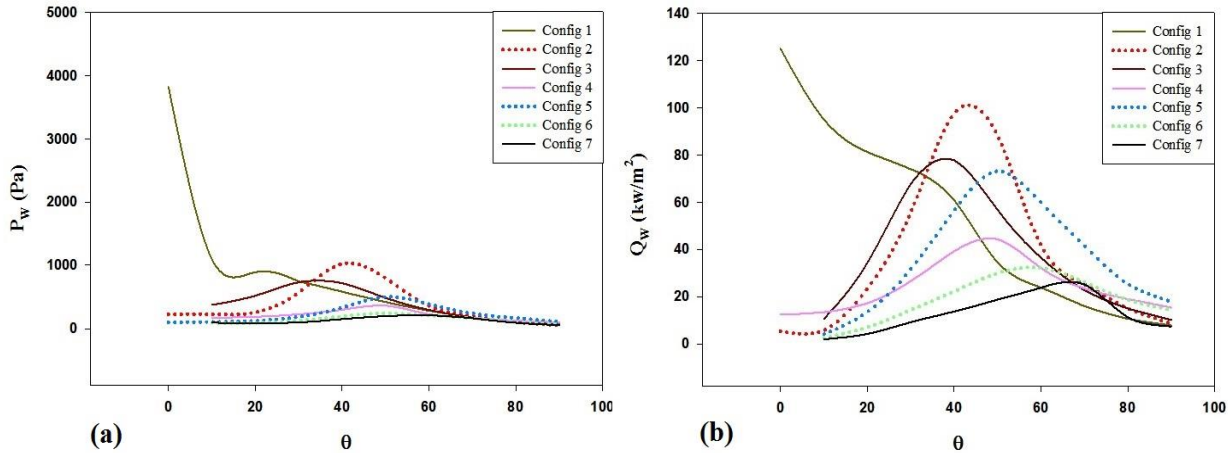| Model	Config 1	Config 2	Config 3	Config 4	Config 5	Config 6
G	72.1%	70.7%	67.04%	52.1%	56.3%	20.1%

Fig. 12 Comparison of (a) pressure dissemination and (b) heat flux dissemination on the blunt nose walls for seven geometrical models

In order to study the percentage of drag deduction in each configuration to the configuration of a single blunt nose (configuration 1), the k parameter is defined as below:

$$K = \frac{C_{dall,Config\ n} - C_{dall,Config\ 1}}{C_{dall,Config\ 1}} \times 100 \qquad (19)$$

In Table 3, the values of k are suggested for various configurations. It is obvious that configuration 7 has the most performance in the deduction of drag factor compared to the others.

Furthermore, to evaluate the total drag factor deduction of configuration 7 to configurations 1 to 6, parameter G is defined as:

$$G = \frac{C_{dall,Config\ n} - C_{dall,Config\ 7}}{C_{dall,Config\ n}} \times 100 \qquad (20)$$

In Table 4, the values of parameter G for configuration 7 to other configurations are proposed.

In Fig. 12, the pressure and heat flux dissemination on the blunt nose walls are compared with each other in various configurations. It is observed that the overall trend of pressure and heat flux deviations along the blunt nose surface is similar in different modes so that the pressure and heat flux curves reach the climax point and finally drop. Accordingly, regarding the displacement of the stagnation point to the mentioned colliding point, the maximum pressure and heat flux are achieved in this zone and the other areas of the blunt nose experience lower pressure and heat flux. As the fig shows, in different configurations, the location of the stagnation point deviates from the nose's pin. Based on Fig. 9 and charts in Fig. 12, it is concluded that with the shear layer deviation

to the blunt nose pin, the location of the collision and the stagnation point event are changed as a result. Therefore, the maximum pressure position in the charts has been forwarded to the nose's pin. In configuration 1, the pressure and heat flux charts experience a descending trend. This stems from the formation of a stagnation point at zero angle and considerable growth in the pressure and heat flux at this point. In this case, by moving toward the blunt nose surface, the total pressure decreases, and the heat flux goes under a descending trend. Based on Fig. 12, it can be concluded that the minimum pressure dissemination and heat flux on the blunt nose walls are dedicated to configuration 7.

Figure 13 shows the comparison of the maximum pressure and the maximum heat flux on the blunt nose walls for seven geometrical models with different configurations. It is observed that the maximum pressure and the maximum heat flux have significant effects on drag and total aerodynamic heating. This fig also shows the impact of the reconnect shock intensity and shock-shock interaction on the blunt nose walls.

Accordingly, the maximum pressure and maximum heat flux values of each configuration are substantial to evaluate the effectiveness of the other six configurations compared to the blunt nose configuration.

According to Fig. 13, configuration 7 has generated the most deduction in the maximum pressure and maximum heat flux among the other configurations.

Figure 14 shows the Stanton number dissemination in seven different configurations on the blunt nose wall. As seen in Fig. 14, it is clear that the value of this parameter
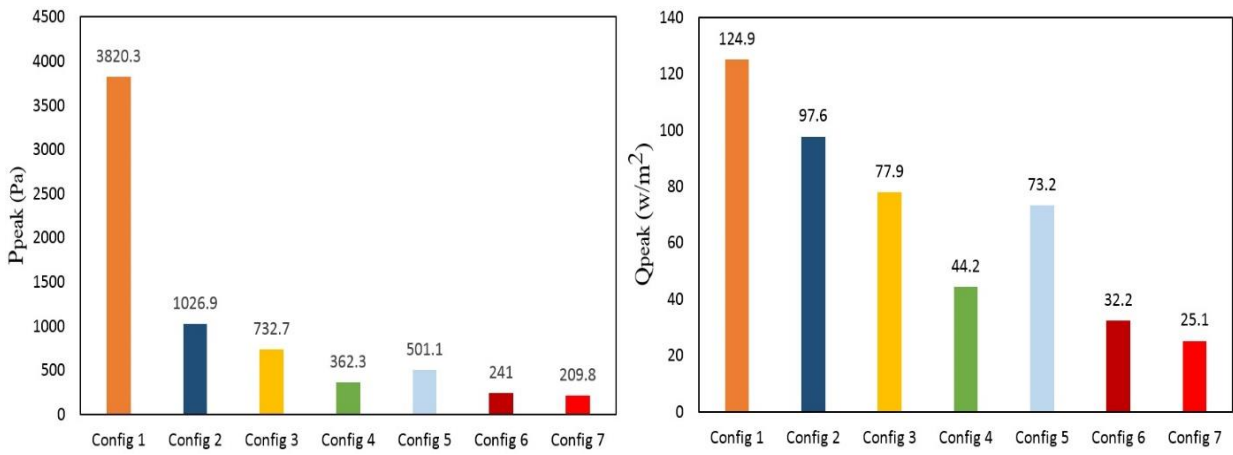
Fig. 13 comparison of (a) maximum pressure and (b) maximum heat flux on the blunt nose walls for seven configuration models
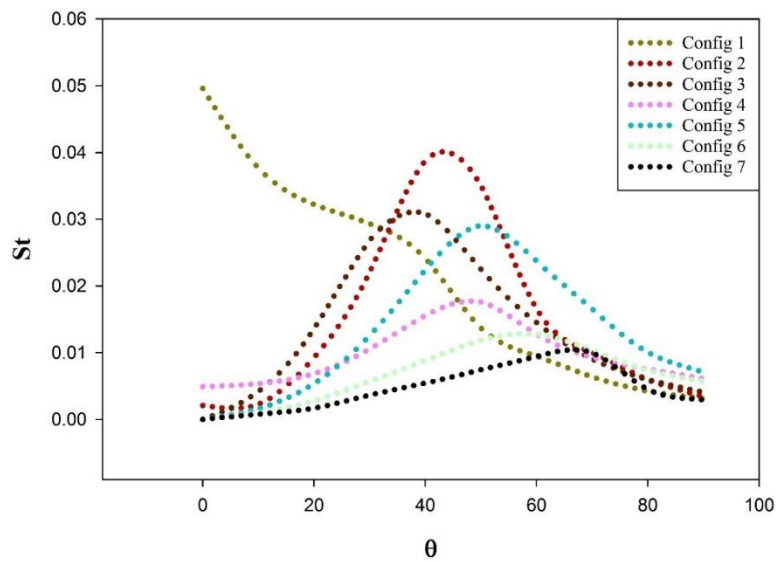

Fig. 14 Comparison of St Disseminations on the blunt nose walls for seven configuration models

on the wall of the blunt nose and stagnation point in the mode without jet and aerospike (configuration 1) shows higher values than in other modes. But by adding a spike or counter flow jet (configurations 2 and 3), the Stanton number increments up to a maximum value and then decreases. The maximum value created in each case is created from the reconnect shock wave that is obtained from the impact of the shear layer on the body of the blunt nose. Examining mode 3 compared to the second mode shows that Stanton maximum values in mode 3 (with counter flow jet) are much lower than configuration two (with spike). This is because the reconnect shock wave in configuration 2 (with spike) is much stronger than configuration 3 and is closer to the nose surface. By placing the combination of spike and aerodisk (configuration 4) and spike and counter flow jet (configuration 5), the Stanton number dissemination on the blunt nose wall shows lower values than the previous three configurations (configurations 1, 2, and 3). Also, the reconnect shock wave in configurations 4 and 5 is much weaker than in configurations 1, 2, and 3 and is further away from the nose surface. Considering the results of

configurations 4 and 5, the necessity of using a jet and aerospike is determined. Accordingly, in configuration 6 of the spike, a smooth surface aerodisk, and counter flowing root jet, and in configuration 7 of the spike, multi-row discs (three flat aerodisks and a conical aerodisk) and an counter flowing root jet have been used to affect the to show the merit of the combined methods. As can be seen, the Stanton number dissemination diagram and the maximum value of the Stanton number in configuration 6 are much lower than in the first 5 configurations. This is because the reconnect shock wave in configuration 6 is much weaker and farther from the nose surface. Configuration 7 shows the greatest deduction in maximum Stanton number and reconnect shock wave intensity among other configurations. Furthermore, in configuration 7 the reconnect shock wave is further away from the nose surface than in the other 6 configurations. Therefore, the current research recommends the use of the combined thermal protection system of configuration 7, which is a combination of multi-row disks, spike, and counter flowing root jet method.

Table. 5 Performance of the maximum pressure deduction for each configuration compared with configuration 1

Model	Config 2	Config 3	Config 4	Config 5	Config 6	Config 7
H	73.1%	80.6%	91.4%	86.8%	93.6%	94.5%

Table. 6 Performance of the maximum heat flux deduction for each configuration compared with configuration 1

Model	Config 2	Config 3	Config 4	Config 5	Config 6	Config 7
I	21.7%	37%	64.5%	41.1%	74.1%	79.9%

Table. 7 Deduction performance of maximum pressure for configuration 7 compared with other configurations

Model	Config 1	Config 2	Config 3	Config 4	Config 5	Config 6
F	94.5%	79.5%	71.3%	42.09%	58.1%	12.9%

Table. 8 Deduction performance of maximum heat flux for configuration 7 compared with other configurations

Model	Config 1	Config 2	Config 3	Config 4	Config 5	Config 6
M	79.9%	67.6%	41.7%	43.2%	65.7%	22.04%

In order to better comparison of the results, the deduction percentage of the maximum pressure and maximum heat flux in various configurations compared with the reference mode (blunt nose configuration) are shown in Tables 5 and 6. To investigate the deduction percentage of the maximum pressure and maximum heat flux in each configuration compared to configuration 1 (single blunt nose), are defined as the H and I such as below:

$$H = \frac{P_{\text{Maximum,Config n}} - P_{\text{Maximum,Config 1}}}{P_{\text{maximum,Config 1}}} \qquad (21)$$

$$I = \frac{Q_{\text{Maximum,Config n}} - Q_{\text{Maximum,Config 1}}}{Q_{\text{maximum,Config 1}}} \qquad (22)$$

In table.7, the values of H parameter are suggested for different configurations in relation to configuration 1. It is obvious that configuration 7 has the highest performance in the deduction of maximum pressure compared with other configurations.

In Table 8, the values of parameter I are suggested for different configurations compared with configuration 1. It is obvious that configuration 7 has the highest performance in the deduction of maximum heat flux compared with other configurations.

Furthermore, to evaluate the deduction percentage of maximum pressure and maximum heat flux on configuration 7 compared with configurations 1 to 6, parameters of F and M are defined as:

$$F = \frac{P_{\text{Maximum.Config n}} - P_{\text{Maximum.Config 7}}}{P_{\text{maximum.Config } n}} \times 100 \qquad (23)$$

$$M = \frac{Q_{\text{Maximum.Config n}} - Q_{\text{Maximum.Config 1}}}{Q_{\text{maximum.Config 1}}} \times 100 \qquad (24)$$

In Tables 7 and 8, F and M parameters are presented for configuration 7 compared to the other six configurations.

According to the presented results, it is defined that applying the various configurations on the blunt nose has a positive and determining effect on the deduction of drag and aerodynamic heating for the blunt nose. It is observed that although adding the spike, aerodisk and counter flow jet to the blunt nose detachedly has acceptable deduction effects on drag factor and heat flux, but simultaneously using several approaches, such as configuration 7, significantly decreases drag factor and aerodynamic heating, which is very desirable.

6. CONCLUSION

In this research, the effects of applying seven various control approaches on the flow behavior on a blunt nose were studied. To accomplish this purpose, seven different configurations were employed, and their effects were evaluated. The most important conclusions are:

The results showed that all the used configurations caused the shock wave formation point to get farther than the nose. The position of shock wave formation actually equals the stagnation point location, which has the highest temperature, and moving farther than the nose's tip causes the pressure and heat transfer values to be diminished. With moving away from the shock wave formation point, the flow velocity falls down near the nose's walls. As a consequence, a significant deduction in aerodynamic heating and drag is observed on the nose.

Using a combination of counter flow jet and aerodisk in a configuration has higher effectiveness on drag and aerodynamic heating than using them detachedly.

In hybrid configurations (including spike, aerodisk, etc.), bow shock, and reconnect, a large vortex zone is created in front of the blunt nose, and the shear layer is produced. The hybrid configurations (configurations 6 and 7) have a weaker reconnect shock compared with the other configurations and also have more effectiveness in the deduction of drag and aerodynamic heating.

With comparing the results of the seven obtained configurations, it was observed that the effectiveness of the different configurations on the deduction of drag and aerodynamic heating are as follows: 1- configuration 7, 2-

configuration 6 3- configuration 4, 4- configuration 5, 5- configuration 3, 6- configuration 2, and 7- configuration 1

The results showed that in terms of drag and aerodynamic heating, configuration 7, with a drag factor of 0.2699, maximum pressure of 209.8 Pa, and maximum heat flux of 25.1 kW/m^2, operates better than the other configurations. Also, the deduction percentage of drag factor, maximum pressure, and maximum heat flux of configuration 7 compared to configuration 1 (blunt nose) are %72.1, %94.5, and %79.9, respectively, which is a significant deduction in drag and aerodynamic heating applied to the blunt-body.

In the hybrid approach of multi-row disks (MRDs) and counter flow jet (configuration 7), flat face aerodisks which are located as steps with a tangential slope on the nose, cause the compression of the oblique shock produced by the spiked tip conical aerodisks and also leads to a decrease in the hypersonic speed of the free stream to diminish the intensity of the reconnect shock. In addition, the low-temperature gas of the counter flow jet refrigerates the blunt nose directly, and enlarging the vortex zone makes the reconnect shock collide the blunt nose at the downstream and a farther distance.

According to the findings, Configuration 7 demonstrated more positive and significant effects on the free stream flow field compared to the other six configurations. It exhibited a higher deduction in drag and aerodynamic heating. The primary reason for this improvement in Configuration 7 is the presence of a conical shock-wave configuration, which transforms the primary oblique shock wave into an inclined shock wave, leading to flow detachment. Additionally, three flat aerodisks redirect the detached flow upward and decrease its velocity. The reconnect shock wave is also diverted away from the blunt nose, resulting in a deduction in its intensity. Furthermore, the inclusion of flat aerodisks in the cavities along the spike creates four low-pressure and low-energy vortical regions. The counter-jet penetrates into the oblique shock wave generated by the spike and the four flat aerodisks, further diminishing the intensity of the reconnect shock wave. As a result, a large longitudinal and transverse vertical region is formed in front of the blunt nose. Moreover, the low-temperature gas released by the jet directly cools the blunt nose. Therefore, Configuration 7 not only significantly reduces the intensity of the reconnect shock wave but also influences its occurrence further away from the blunt nose, closer to the shoulder of the blunt nose. Additionally, it directly cools the blunt nose. Based on these findings, Configuration 7 is suggested as the most effective configuration among all proposed configurations in terms of reducing drag and aerodynamic heating.

CONFLICT OF INTEREST

The authors declare that they have no known competing financial interests or personal relationships that could have appeared to influence the work reported in this paper.

AUTHOR CONTRIBUTION:

REFERENCES

Ahmed, M., & Qin, N. (2011). Recent advances in the aerothermodynamics of spiked hypersonic vehicles. *Progress in Aerospace Sciences*, *47*(6), 425-449. https://doi.org/10.1016/j.paerosci.2011.06.001

Ahmed, M. Y., & Qin, N. (2014). Investigation of flow asymmetry around axi-symmetric spiked blunt bodies in hypersonic speeds. *The Aeronautical Journal*, *118*(1200), 169-179. https://doi.org/10.1017/S0001924000009052

Ahmed, M. Y., & Qin, N. (2020). Forebody shock control devices for drag and aero-heating reduction: A comprehensive survey with a practical perspective. *Progress in Aerospace Sciences*, *112*, 100585. https://doi.org/10.1016/j.paerosci.2019.100585

Alexander, S. R. (1947). *Results of Tests of determine the effect of a conical windshield on the drag of a bluff body at supersonic speeds*. NACA PM No. L6KO8a

Anderson Jr, J. D., Lewis, M. J., Kothari, A. P., & Corda, S. (1991). Hypersonic waveriders for planetary atmospheres. *Journal of Spacecraft and Rockets*, *28*(4), 401-410. https://doi.org/10.2514/3.26259

Betelin, V., Kushnirenko, A., Smirnov, N., Nikitin, V., Tyurenkova, V., & Stamov, L. (2018). Numerical investigations of hybrid rocket engines. *Acta Astronautica*, *144*, 363-370. https://doi.org/10.1016/j.actaastro.2018.01.009

Bhamare, D. K., Rathod, M. K., & Banerjee, J. (2020). Numerical model for evaluating thermal performance of residential building roof integrated with inclined phase change material (PCM) layer. *Journal of Building Engineering*, *28*, 101018. https://doi.org/10.1016/j.jobe.2019.101018

Bogdonoff, S. M., & Vas, I. E. (1959). Preliminary investigations of spiked bodies at hypersonic speeds. *Journal of the Aerospace Sciences*, *26*(2), 65-74. https://doi.org/10.2514/8.7945

Chinnappan, A. K., Malaikannan, G., & Kumar, R. (2017). Insights into flow and heat transfer aspects of hypersonic rarefied flow over a blunt body with aerospike using direct simulation Monte-Carlo approach. *Aerospace Science and Technology*, *66*, 119-128. https://doi.org/10.1016/j.ast.2017.02.024

Crawford, D. H. (1959). *Investigation of the flow over a spiked-nose hemisphere-cylinder at a Mach number of 6.8*. National Aeronautics and Space Administration. NASA TN D-118

Dem'ianov, I. A., & Shmanenkov, V. (1960). Investigation of reverse flows in the region of separation of the turbulent boundary layer. *Journal of Applied*

Mathematics and Mechanics, *24*(2), 340-343. https://doi.org/10.1016/0021-8928(60)90037-X

Desai, S., Prakash K, V., Kulkarni, V., & Gadgil, H. (2020). Universal scaling parameter for a counter jet drag reduction technique in supersonic flows. *Physics of Fluids*, *32*(3), 036105. https://doi.org/10.1063/1.5140029

Eghlima, Z., Mansour, K., & Fardipour, K. (2018). Heat transfer reduction using combination of spike and counterflow jet on blunt body at high Mach number flow. *Acta Astronautica*, *143*, 92-104. https://doi.org/10.1016/j.actaastro.2017.11.012

Fujii, K., Tsuda, S., Koyama, T., & Hirabayashi, N. (2013). *Oscillation of bow-shock waves at hypersonic speeds.* 43rd AIAA Fluid Dynamics Conference. https://doi.org/10.2514/6.2013-3103

Guenther, R. A., & Reding, J. P. (1977). Fluctuating pressure environment of a drag reduction spike. *Journal of Spacecraft and Rockets*, *14*(12), 705-710. https://doi.org/10.2514/3.57253

Han, G., & Jiang, Z. (2018). Hypersonic flow field reconfiguration and drag reduction of blunt body with spikes and sideward jets. *International Journal of Aerospace Engineering*, *2018*. https://doi.org/10.1155/2018/7432961

Hayashi, K., Aso, S., & Tani, Y. (2005). *Numerical study of thermal protection system by opposing jet*. 43rd AIAA Aerospace Sciences Meeting and Exhibit. https://doi.org/10.2514/6.2005-188

Hayashi, K., Aso, S., & Tani, Y. (2006). Experimental study on thermal protection system by opposing jet in supersonic flow. *Journal of Spacecraft and Rockets*, *43*(1), 233-235. https://doi.org/10.2514/1.15332

Holden, M. S. (1966). Experimental studies of separated flows at hypersonic speeds. I-Separated flows over axisymmetric spiked bodies. *AIAA Journal*, *4*(4), 591-599. https://doi.org/10.2514/3.3494

Huang, J., & Yao, W. X. (2019). A novel non-ablative thermal protection system with combined spike and opposing jet concept. *Acta Astronautica*, *159*, 41-48. https://doi.org/10.1016/j.actaastro.2019.02.005

Huang, J., & Yao, W. X. (2020). Hypersonic drag reduction mechanism of a novel combinational spike and multi-opposing jets aerodynamic configuration. *Acta Astronautica*, *171*, 245-256. https://doi.org/10.1016/j.actaastro.2020.03.009

Huang, J., Yao, W. X., & Shan, X. Y. (2019). Numerical investigation on drag and heat reduction mechanism of combined spike and rear opposing jet configuration. *Acta Astronautica*, *155*, 179-190. https://doi.org/10.1016/j.actaastro.2018.11.039

Huang, W., Zhang, R. R., Yan, L., Ou, M., & Moradi, R. (2018). Numerical experiment on the flow field properties of a blunted body with a counterflowing jet in supersonic flows. *Acta Astronautica*, *147*, 231-240. https://doi.org/10.1016/j.actaastro.2018.04.018

Ji, C., Liu, B., Huang, W., Li, S. B., & Yan, L. (2021). Investigation on the drag reduction and thermal protection properties of the porous opposing jet in the supersonic flow: A parametric study with constant mass flow rate. *Aerospace Science and Technology*, *118*, 107064. https://doi.org/10.1016/j.ast.2021.107064

Kushnirenko, A., Stamov, L., Tyurenkova, V., Smirnova, M., & Mikhalchenko, E. (2021). Three-dimensional numerical modeling of a rocket engine with solid fuel. *Acta Astronautica*, *181*, 544-551. https://doi.org/10.1016/j.actaastro.2021.01.028

Li, S., Huang, W., Lei, J., & Wang, Z. (2018). Drag and heat reduction mechanism of the porous opposing jet for variable blunt hypersonic vehicles. *International Journal of Heat and Mass Transfer*, *126*, 1087-1098. https://doi.org/10.1016/j.ijheatmasstransfer.2018.06.054

Love, E. S. (1952). *The effects of a small jet of air exhausting from the nose of a body of revolution in supersonic flow*. National Advisory Committee for Aeronautics. NACA RM L52I19a

Ma, K., Li, Y., Zhu, L., Chen, X., & Zhou, C. (2020). Spike root oblique jet effect on drag and heat load reduction performance for hypersonic vehicles. *Acta Astronautica*, *177*, 588-603. https://doi.org/10.1016/j.actaastro.2020.08.023

Mair, W. (1952). LXVIII. Experiments on separation of boundary layers on probes in front of blunt-nosed bodies in a supersonic air stream. *The London, Edinburgh, and Dublin Philosophical Magazine and Journal of Science*, *43*(342), 695-716. https://doi.org/10.1080/14786440708520987

Mansour, K., & Khorsandi, M. (2014). The drag reduction in spherical spiked blunt body. *Acta Astronautica*, *99*, 92-98. https://doi.org/10.1016/j.actaastro.2014.02.009

Marley, C. D., & Riggins, D. W. (2011). Numerical study of novel drag reduction techniques for hypersonic blunt bodies. *AIAA Journal*, *49*(9), 1871-1882. https://doi.org/10.2514/1.J050681

Mehta, R. (2000). Numerical heat transfer study over spiked blunt bodies at Mach 6.8. *Journal of Spacecraft and Rockets*, *37*(5), 700-703. https://doi.org/10.2514/2.3622

Mehta, R. (2002). Numerical analysis of pressure oscillations over axisymmetric spiked blunt bodies at Mach 6.80. *Shock Waves*, *11*(6), 431-440. https://doi.org/10.1007/s001930200127

Meng, Y. S., Yan, L., Huang, W., & Wang, Z. W. (2021). Fluid-thermal coupled investigation on the combinational spike and opposing/lateral jet in hypersonic flows. *Acta Astronautica*, *185*, 264-282. https://doi.org/10.1016/j.actaastro.2021.05.022

Menter, F. R. (1994). Two-equation eddy-viscosity turbulence models for engineering applications. *AIAA*

Journal, *32*(8), 1598-1605. https://doi.org/10.2514/3.12149

Milicev, S. S., & Pavlovic, M. D. (2002). Influence of spike shape at supersonic flow past blunt-nosed bodies: experimental study. *AIAA Journal*, *40*(5), 1018-1020. https://doi.org/10.2514/2.1745

Motoyama, N., Mihara, K., Miyajima, R., Watanuki, T., & Kubota, H. (2001). *Thermal protection and drag reduction with use of spike in hypersonic flow.* 10th AIAA/NAL-NASDA-ISAS International Space Planes and Hypersonic Systems and Technologies Conference. https://doi.org/10.2514/6.2001-1828

Narayana, G., & Selvaraj, S. (2020). Attenuation of pulsation and oscillation using a disk at mid-section of spiked blunt body. *Physics of Fluids*, *32*(11), 116106. https://doi.org/10.1063/5.0024649

Ou, M., Yan, L., Huang, W., & Zhang, T. T. (2019). Design exploration of combinational spike and opposing jet concept in hypersonic flows based on CFD calculation and surrogate model. *Acta Astronautica*, *155*, 287-301. https://doi.org/10.1016/j.actaastro.2018.12.012

Panaras, A. G., & Drikakis, D. (2009). High-speed unsteady flows around spiked-blunt bodies. *Journal of Fluid Mechanics*, *632*, 69-96. https://doi.org/10.1017/S0022112009006235

Piland, R. O., & Putland, L. W. (1956). *Zero-Lift drag of several conical and blunt nose shapes obtained in free flight at mach numbers of 0.7 to 1.3*. RM L54A27

Qin, Q., & Xu, J. (2019). Numerical evaluation of aerodome and cooling jet for aeroheating reduction. *Aerospace Science and Technology*, *86*, 520-533. https://doi.org/10.1016/j.ast.2019.01.046

Qin, Q., Xu, J., & Guo, S. (2018). Reduction of aeroheating and drag using lateral/oblique/opposing jet on aerodome. *Journal of Spacecraft and Rockets*, *55*(2), 523-527. https://doi.org/10.2514/1.A34041

Qu, F., Sun, D., Bai, J., Zuo, G., & Yan, C. (2018). Numerical investigation of blunt body's heating load reduction with combination of spike and opposing jet. *International Journal of Heat and Mass Transfer*, *127*, 7-15. https://doi.org/10.1016/j.ijheatmasstransfer.2018.06.154

Raman, S. K., Kexin, W., Kim, T. H., Suryan, A., & Kim, H. D. (2020). Effects of flap on the reentry aerodynamics of a blunt cone in the supersonic flow. *International Journal of Mechanical Sciences*, *176*, 105396. https://doi.org/10.1016/j.ijmecsci.2019.105396

Rashid, S., Nawaz, F., Maqsood, A., Riaz, R., & Salamat, S. (2019). Shock reduction through opposing jets— aerodynamic performance and flight stability perspectives. *Applied Sciences*, *10*(1), 180. https://doi.org/10.3390/app10010180

Rashid, S., Nawaz, F., Maqsood, A., Salamat, S., Riaz, R., Dala, L., & Ahmad, R. (2021). Modeling and analysis of shock reduction through counterflow plasma jets. *Mathematical Problems in Engineering*, *2021*. https://doi.org/10.1155/2021/5592855

Renane, R., Allouche, R., Zmit, O., & Bouchama, B. (2022). *Aero Heating Optimization of a Hypersonic Thermochemical Non-Equilibrium Flow around Blunt Body by Application of Opposing Jet and Blunt Spike.* Hypersonic Vehicles-Applications, Recent Advances, and Perspectives. IntechOpen. https://doi.org/10.5772/intechopen.101659

Romeo, D. J. (1963). *Exploratory investigation of the effect of a forward-facing jet on the bow shock of a blunt body in a Mach number 6 free stream. NASA TN*, TN D-1605. NASA TN D-1605

Sahoo, D., Das, S., & Cohen, J. (2019). *Effect of body nose fairing on the unsteady flow characteristics over spiked flat faced cylinder at supersonic speed.* AIAA Scitech 2019 Forum. https://doi.org/10.2514/6.2019-2316

Sahoo, D., Das, S., Kumar, P., & Prasad, J. (2016). Effect of spike on steady and unsteady flow over a blunt body at supersonic speed. *Acta Astronautica*, *128*, 521-533. https://doi.org/10.1016/j.actaastro.2016.08.005

Saravanan, S., Jagadeesh, G., & Reddy, K. (2009). Investigation of missile-shaped body with forward-facing cavity at Mach 8. *Journal of Spacecraft and Rockets*, *46*(3), 577-591. https://doi.org/10.2514/1.38914

Seiler, F., Srulijes, J., Gimenez Pastor, M., & Mangold, P. (2007). *Heat fluxes inside a cavity placed at the nose of a projectile measured in a shock tunnel at Mach 4.5.* New results in numerical and experimental fluid mechanics VI. Springer. https://doi.org/10.1007/978-3-540-74460-3_38

Sharma, K., & Nair, M. T. (2020). Combination of counterflow jet and cavity for heat flux and drag reduction. *Physics of Fluids*, *32*(5), 056107. https://doi.org/10.1063/1.5143521

Shen, B., Liu, W., & Yin, L. (2018). Drag and heat reduction efficiency research on opposing jet in supersonic flows. *Aerospace Science and Technology*, *77*, 696-703. https://doi.org/10.1016/j.ast.2018.03.051

Silton, S. I., & Goldstein, D. B. (2005). Use of an axial nose-tip cavity for delaying ablation onset in hypersonic flow. *Journal of Fluid Mechanics*, *528*, 297-321. https://doi.org/10.1017/S0022112004002460

Stalder, J. R., & Nielsen, H. V. (1954). *Heat transfer from a hemisphere-cylinder equipped with flow-separation spikes*. NACA-TN-3287

Sundarraj, V., Sundarraj, K., & Kulkarni, P. S. (2021). Thermo-fluid analysis of supersonic flow over ballistic shaped bodies with multiple aero-disk spike configurations. *Acta Astronautica*, *180*, 292-304. https://doi.org/10.1016/j.actaastro.2020.12.022

Tahani, M., Karimi, M., Motlagh, A. M., & Mirmahdian, S. (2013). Numerical investigation of drag and heat reduction in hypersonic spiked blunt bodies. *Heat and Mass Transfer*, *49*(10), 1369-1384. https://doi.org/10.1007/s00231-013-1173-4

Tembhurnikar, P. V., Jadhav, A. T., & Sahoo, D. (2020). Effect of intermediate aerodisk mounted sharp tip spike on the drag reduction over a hemispherical body at Mach 2.0. *FME Transactions*, *48*(4), 779-786. https://doi.org/10.5937/fme2004779T

Vali, S. E., & Abbasi, S. (2022). Hypersonic drag and heat reduction mechanism of a new hybrid method of spike, multi-row discs and opposing jets aerodynamic configuration. *International Journal of Heat and Mass Transfer*, *194*, 123034. https://doi.org/10.1016/j.ijheatmasstransfer.2022.123034

Wang, Z., & Zhang, X. (2022). Parametric research on drag reduction and thermal protection of blunt-body with opposing jets of forward convergent nozzle in supersonic flows. *Acta Astronautica*, *190*, 218-230. https://doi.org/10.1016/j.actaastro.2021.10.021

Xie, W., Luo, Z., Hou, L., Zhou, Y., Liu, Q., & Peng, W. (2021). Characterization of plasma synthetic jet actuator with Laval-shaped exit and application to drag reduction in supersonic flow. *Physics of Fluids*, *33*(9), 096104. https://doi.org/10.1063/5.0064533

Yadav, R., Bodavula, A., & Joshi, S. (2018). Numerical investigation of the effect of disk position on the aerodynamic heating and drag of a spiked blunt body in hypersonic flow. *The Aeronautical Journal*, *122*(1258), 1916-1942. https://doi.org/10.1017/aer.2018.109

Yamauchi, M., Fujii, K., & Higashino, F. (1995). Numerical investigation of supersonic flows around a spiked blunt body. *Journal of Spacecraft and Rockets*, *32*(1), 32-42. https://doi.org/10.2514/3.26571

Zhang, J., Ma, H., & Qin, Y. (2017). *Experimental investigation on flow characteristic of combination of forward-facing jet and spike.* 21st AIAA International Space Planes and Hypersonics Technologies Conference. https://doi.org/10.2514/6.2017-2402

Zhang, W., Wang, X., Zhang, Z., Han, F., & Zhao, S. (2022). Heat and drag reduction of single and combined opposing jets in hypersonic nonequilibrium flows. *Aerospace Science and Technology*, *121*, 107194. https://doi.org/10.1016/j.ast.2021.107194

Zhong, K., Yan, C., Chen, S. S., Zhang, T. X., & Lou, S. (2019). Aerodisk effects on drag reduction for hypersonic blunt body with an ellipsoid nose. *Aerospace Science and Technology*, *86*, 599-612. https://doi.org/10.1016/j.ast.2019.01.027

Zhu, L., Chen, X., Li, Y., Musa, O., & Zhou, C. (2018). Investigation of drag and heat reduction induced by a novel combinational lateral jet and spike concept in supersonic flows based on conjugate heat transfer approach. *Acta Astronautica*, *142*, 300-313. https://doi.org/10.1016/j.actaastro.2017.11.001

Zhu, L., Li, Y., Chen, X., Gong, L., Xu, J., & Feng, Z. (2019). Novel combinational aerodisk and lateral jet concept for drag and heat reduction in hypersonic flows. *Journal of Aerospace Engineering*, *32*(1), 04018133. https://doi.org/10.1061/(ASCE)AS.1943-5525.0000966

Zhu, L., Tian, X., Li, W., Yan, M., Tang, X., & Huang, M. (2021). Nonablative dual-jet strategy for drag and heat reduction of hypersonic blunt vehicles. *Journal of Aerospace Engineering*, *34*(5), 04021052. https://doi.org/10.1061/(ASCE)AS.1943-5525.0001290